# Characterizing Microearthquakes Induced by Hydraulic Fracturing with Hybrid Borehole DAS and Three-Component Geophone Data

Zhen-dong Zhang, Malcolm C. A. White, Tong Bai, Hongrui Qiu and Nori Nakata

*Abstract*—Fluids injected during hydraulic fracturing (fracking) in unconventional shale oil and gas reservoirs, geothermal system enhancement, wastewater disposal, and carbon capture and storage can induce microearthquakes. The spatiotemporal distribution of induced earthquakes is often used to trace the growth of fractures in target layers and guides production. We analyze microseismicity behavior induced by fracking in the Montney Formation, one of the largest unconventional oil and gas reservoirs in North America. An optical fiber deployed in a horizontal well provides extensive spatial sampling and data coverage for microseismic imaging. We design median and F-k filters to predict instrumental and random noise and further suppress them by adaptive noise subtraction. An elliptical vertical transverse isotropic (VTI) velocity model is derived from the Backus-averaged well-log sonic data and is modified to match the microseismic wavefronts by a grid search. We image 41 previously cataloged microearthquakes recorded by DAS using Geometric-mean Reverse Time Migration. We find that the fiber geometry's lack of 2D/3D variations increases the non-uniqueness of the image point location, and the P-wave particle motions derived from 3C geophones data can effectively eliminate the location ambiguity. The spatiotemporal distribution of our updated locations agrees with the fracking schedule. Predicted P- and S-wave traveltimes from the updated locations also match with the observed waveforms. Analyzing data sensitivity to source locations confirms the potential limitations imposed on source imaging by the geometry of borehole observations and shows that relocation accuracy is directionally dependent. We also investigate the feasibility of estimating source focal mechanisms using realistic DAS and geophone observations. Our study provides guidance for characterizing microearthquake sources and optimizing observation geometry for unconventional reservoirs.

*Index Terms*—DAS, microearthquake, focal mechanism, elastic, VTI.

## I. INTRODUCTION

**M**ICROEARTHQUAKES that are imperceptible to humans without specialized sensors—are routinely generated during hydraulic fracturing [1], [2]. They are generally localized at pre-existing fault surfaces or are created within volumes of newly fractured rock. Imaging, or otherwise characterizing, microseismic sources can thus be used to detect fault slip and monitor activity related to enhancing subsurface resource production [3]–[5]. Characterizing microseismic sources is a typical geophysical inverse problem in which an optimal set of model parameters—including, for example, the focal mechanism, the origin time, and the source location—is sought by minimizing the discrepancy between observed and predicted data [6]–[8]. Recovering the entire set of source-related model parameters requires exhaustive observational coverage, which is prohibitively expensive in practice. Indeed, different components of seismic waveform data have variable sensitivities to parameters that are used to characterize the source [9]. The origin time and source location directly influence the arrival time of seismic waves, while the focal mechanism mainly affects the dynamic information of the recorded waveform data. As a remedy, simplified earthquake models with reduced numbers of parameters and inversion algorithms that are robust against incomplete data are frequently used in particular applications. Notably, there are inherent trade-offs between inverted seismic sources and earth model parameters [10], [11]. Such trade-offs, however, can be effectively mitigated by a dense spatial sampling of the seismic wavefield, such as those recorded by fiber optic cables using distributed acoustic sensing (DAS) technology. As a result, DAS data are preferable over relatively sparse geophone data for locating microearthquakes [12]–[15]. However, the single-component DAS acquisition can only weakly constrain source locations perpendicular to the fiber or source focal mechanism. The three-component (3C) geophone data, although sparsely distributed, can provide sufficient additional constraints for estimating source locations and focal mechanisms.

Fractures generated during fracking operations are associated with microearthquakes, and accurately locating these microearthquakes is paramount to determining the geometry of growing fracture networks. Because inversion algorithms for determining microearthquake locations mainly rely on matching the kinematics of seismic waves (i.e., ray paths and travel times), estimating such parameters is easier and more robust than dynamic parameters (e.g., the focal mechanism and source-time function). Indeed seismic imaging methods, which are adjoint approximations to the formal inverse, have been widely used to locate microearthquakes [16]–[23]. Time-reversal imaging [16] locates microearthquakes by extracting the zero-lag correlation of back-propagated receiver wavefields. Time-reversal imaging images the radiation pattern of the energy source rather than its location and image quality is thus highly dependent on the acquisition geometry. Incomplete and noisy observations can cause smearing in obtained images; however, this smearing can be effectively suppressed using the geometric-mean imaging condition [18], although

Zhen-dong Zhang, Malcolm C. A. White, Tong Bai and Nori Nakata are with Massachusetts Institute of Technology, Cambridge, MA 02139, USA
Hongrui Qiu and Nori Nakata are with Lawrence Berkeley National Laboratory, Berkeley, CA 94720, USA
Corresponding author: Zhen-dong Zhang, zdzhang@mit.edu

this entails an increase in the computational cost compared with other imaging conditions. Emerging machine learning approaches [23] create a direct mapping between seismic data and the source location and are thus free of source smearing. Among these methods, wave-equation-based imaging requires less human effort and is more tolerant of random noise. However, ray-based imaging is generally less computationally demanding than wave-equation-based imaging. On the other hand, owing to the more complete physical model considered, wave-equation-based imaging methods utilize the full waveform information and can potentially provide better resolution than ray-based imaging. Machine learning methods may learn physics from the provided training data that incorporates both kinematic (ray-based) and dynamic (wave-equation-based) constraints on the imaging process. In this sense, they can be regarded as a unified framework combining ray-based and wave-equation-based methods. Model training, however, is usually time-consuming and sometimes insufficient for general use, but, once trained, source locations can be obtained nearly instantaneously. Notably, for all these imaging methods, the image quality highly depends on the accuracy of the velocity model and input data. It is required that the velocity used for migration should be able to reconstruct the wave-path of the injecting wavefield [24].

The source focal mechanism is secondary to monitoring fracture growth but can effectively indicate the local, in-situ stress field. To invert the focal mechanism, we usually need to match the predicted and observed waveforms in a defined error norm [25]–[27]. The exact matching of the seismic waveforms is always challenging because seismic amplitudes can be affected by many factors other than the source itself [28]. In practice, seismic waves are carefully selected when inverting for focal mechanisms [25]. With a sufficiently accurate velocity model and a complete coverage of observations, we presumably can use an adjoint solution (the first iteration) to approximate the formal inversion (pp.199 in [29]). The subsequent iterations in practice may not significantly improve the focal mechanism estimation from the first iteration (e.g., Figure 6 in [26]).

Fiber co-located, 3C seismic sensors and DAS fibers provide an effective acquisition paradigm for recording sufficient dynamic information in the target area. Complementary subsets of fiber and 3C data can be selected to maximize sensitivity to the particular source parameter being inverted. Sparsely distributed borehole sensors previously posed challenges for location estimation in general, but with DAS emerging as a cost-effective, spatially dense acquisition system, the lack of data coverage is no longer a severe limitation for dynamic microseismic imaging [30]. Owing to its unparalleled dense spatial sampling and affordability, DAS has been used to solve many different geophysical problems. For example, monitoring earthquakes [31], characterizing microseismicity [32], [33], imaging the near-surface [34], mapping urban seismic hazards [35], and monitoring boreholes [15], [36], [37]. DAS, however, measures axial strain (or strain rate) along the fiber and thus has an instrument response that is dependent on the incidence angle of incident energy [38], [39]. Converting DAS measurements to ready-to-use units of particle motion is an open

research topic [40]. DAS data also have different noise patterns from geophone recordings. Several denoising strategies for DAS data have been proposed [40]–[43]; however, relocating microearthquakes imposes minimal requirements on DAS data processing. Constructively stacking seismic wavefields in the imaging process can be achieved with coherent waves, regardless of their units. Thus, we emphasize improving the coherency of waveform traces in data processing and ignoring their physical units for microseismic relocation. 3C geophones record more complete dynamic information of seismic waves emitted from the microearthquakes, and thus are more suitable for estimating source focal mechanisms. With a known source location estimated from the joint DAS and 3C geophone data imaging, the focal mechanism estimation from the 3C data also becomes more precise.

In this paper, we estimate the source location and focal mechanism using the DAS and geophone data jointly, in a two-step sequence. Specifically, we first attenuate the instrumental noise using a de-median filter along the spatial dimension. We then predict noise in the frequency-wavenumber (F-k) domain and apply an adaptive noise subtraction. We demonstrate how to build anisotropic velocity models from well-log sonic data and seismic wavefronts. We briefly review the elastic Geometric-mean Reverse Time Migration methodology and present a modified impedance-kernel imaging condition. A real data set with 41 cataloged events is used to verify the effectiveness and accuracy of the proposed relocation algorithm. We evaluate relocation accuracy through data sensitivity analysis and comparison to the recorded waveform data. Finally, we discuss the feasibility of estimating focal mechanisms using 3C geophone data and conclude. To our best knowledge, the novelty of the paper is summarized as 1) a new imaging scheme using waveform information for locating low-magnitude events, 2) proposed novel time-domain processing algorithms for denoising, and 3) DAS and 3C geophone data are jointly used for microearthquake relocation and focal mechanism inversion.

## II. STUDY SITE

The studied reservoir is located in the Montney Formation of the Western Canadian Sedimentary Basin (Figure 1a), which accounts for about half of the gas supply from Canadian wells [44]. The low permeability of shales in the Montney formation necessitates horizontal drilling and extensive fracking to generate economically viable fluid flow [45], [46]. To this end, four horizontal wells were drilled with 200 m lateral separation in the reservoir [47], and a single fiber optic cable and 24 three-component (3C) geophone sensors were installed in well C (Figure 1b). Zipper fracking was first carried out between wells A and B (the two outermost wells), followed by wells C and D (the two innermost wells; not shown in Figure 1b). In this study, we analyze DAS data extracted for 41 time periods from a 6-hour continuous recording of fracking operations in wells A and B. The dense spatial sampling of the DAS data benefits the relocation of microearthquakes, the traces of which indicate preferred fracture growth directions and thus guide production.
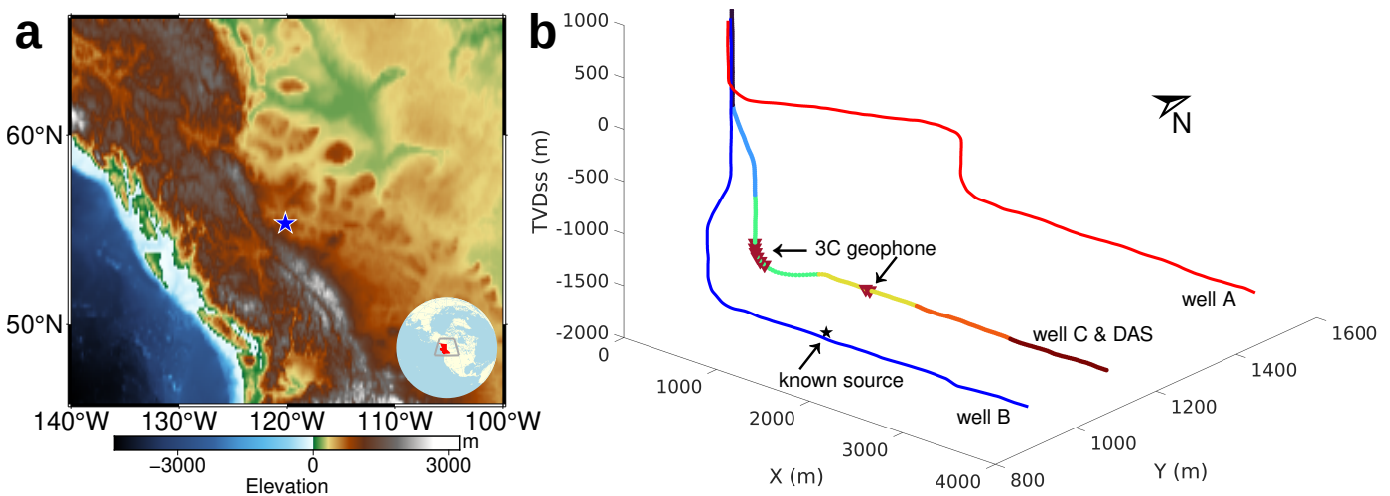
Fig. 1. Location of the study site. The Montney Formation is located in western Canada (a) and is one of the largest unconventional oil and deposition in North America. Hydraulic fracking is required to create flow paths through the ultra-low permeability rocks. Three horizontal wells were piloted to the reservoir layer (b). A DAS acquisition line (color-coded with six subgroups) is deployed in well C, co-located with 24 3C sensors (plotted in every 3 traces). Two fracking stages in wells A and B are analyzed in this study.

## III. DATA PROCESSING

Although DAS acquisition systems offer dense spatial sampling at a low cost, they suffer from certain drawbacks when compared with conventional 3C seismic sensors. One such drawback is the azimuth-dependent sensitivity of DAS, which is determined by the nature of optical fibers. Another drawback is the relatively low coherence at short wavelengths characteristic of tiny events and waveform clipping for large events [40], [48]. Several data processing strategies have been proposed to enhance the signal-to-noise ratio (SNR) of DAS data and convert the measured strain (or strain rate) to units of particle motion (i.e., particle displacement and its time derivatives), which are more familiar to most seismologists [40], [42], [49]. We identify two types of noise in our borehole DAS recordings: a) random noise and b) instrumental noise (Figure 2a). Random noise are supposed to be suppressed by sufficient stacking in wavefield-based imaging. Instrumental noise in our DAS data manifests primarily as vertical and horizontal stripes (i.e., signals with infinite and vanishing slowness, respectively) in a common shot gather (CSG), which may degrade the image quality. To mitigate such non-seismic signals, we design an F-k filter to suppress coherent noise with non-physical slowness (Figure 2b). Our F-k filter, however, has the undesirable side effect of distorting the target signals (Figure 2b). On the other hand, we find that the horizontal stripes can be removed by simply applying a de-median filter in the horizontal/spatial direction (Figure 2c). Thus, after applying the de-median filter, we use the F-k-filtered data as template signals and derive a *matching filter* to further separate the signal and the remaining noise by solving a minimization problem:

$$\min ||\mathbf{d^o}(t) - \mathbf{f}(t) * \mathbf{d^p}(t)||^2 + \epsilon \mathbf{R}(\mathbf{f}(t)), \qquad (1)$$

where $\mathbf{d^o}(t)$ and $\mathbf{d^p}(t)$ denote the de-median and F-k-filtered data, respectively, $\mathbf{f}(t)$ is the desired matching filter that minimizes the data difference, and $\mathbf{R}(\mathbf{f}(t))$ is an L1-norm regularization term weighted by a scalar $\epsilon$ to prevent over-fitting. We solve this minimization problem using regularized non-stationary regression [50].

The signals after denoising are reasonably close to the raw data with the coherent arrivals being clearer (Figure 2d). Figure 3 shows the noise component has been removed during each processing step. The de-median filter primarily removes the instrument noise, but introduces minor waveform distortions (Figure 3a) at the same time. The adaptive filter is designed to further suppress noise and alleviate the distortion of target microseismic signals (Figure 3b). Noise removed by applying both the de-median and the adaptive filters are shown in Figure 3c.

## IV. VELOCITY MODELS

Accurate models of seismic velocity in the subsurface are critical for wavefield-based imaging. Image quality and resolution are heavily influenced by the accuracy of the forward and reconstructed wavefields, which themselves are highly sensitive to errors in the velocity model(s) used for imaging (i.e., migration velocity). Furthermore, seismic waves propagate with direction-dependent velocities (i.e., anisotropy; [51]) in shales. Optimal image quality is often obtained when velocity models are tailored to the frequency band of interest. The available well-log sonic data, however, have much higher frequencies than seismic data. Thin isotropic elastic layers detected by high-frequency sonic logs cause seismic vertical transverse isotropy (VTI) observed at lower frequencies [51], [52]. We use Backus averaging to extract effective-medium models from well logs [53] for vertical P- and S-wave velocities at frequencies suitable for seismic imaging purposes (Figure 4).

The first step of Backus averaging is to calculate a moving average of model parameters,

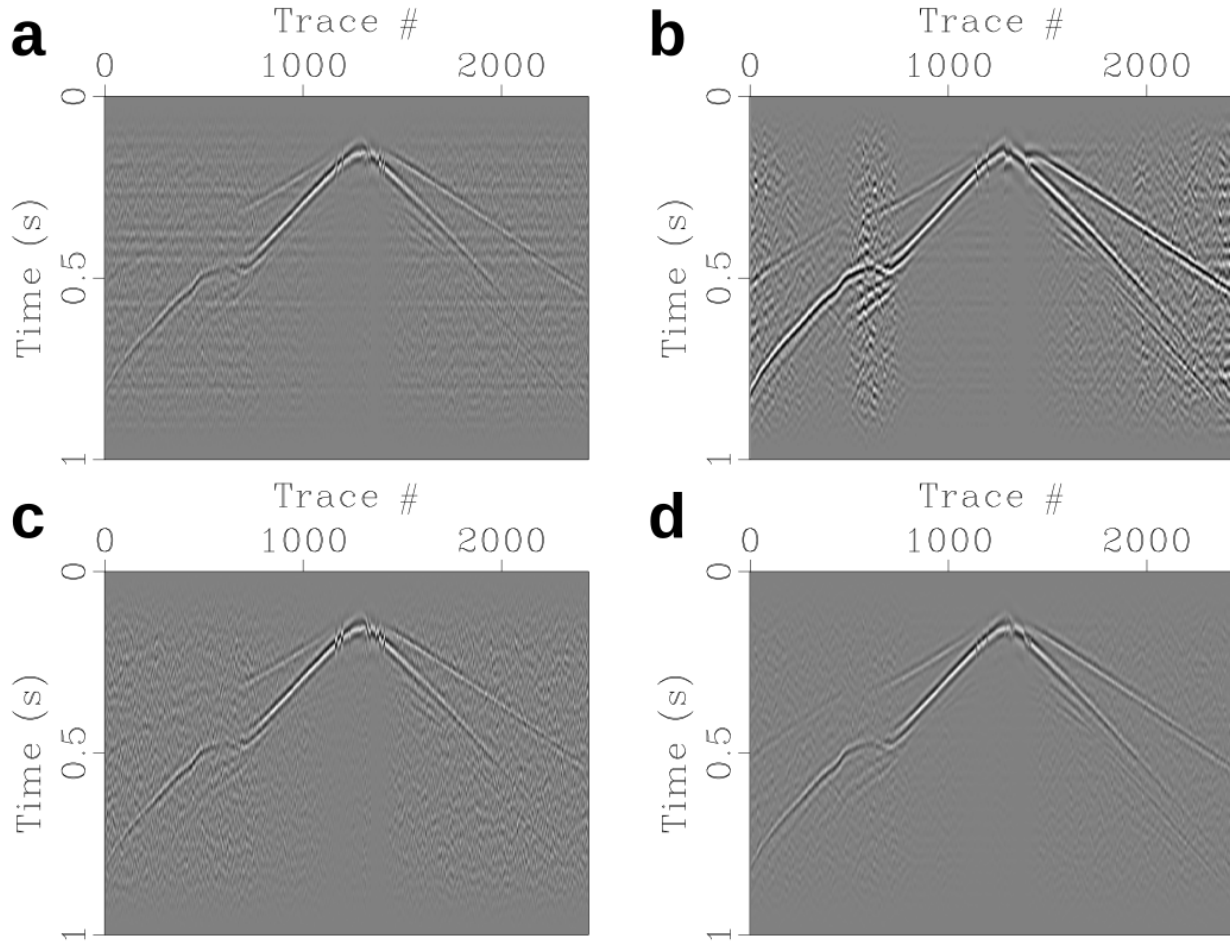$$\langle p \rangle_k = \frac{1}{2h+1} \sum_{i=k-h}^{k+h} p_i, \qquad (2)$$

Fig. 2. Example DAS waveform data. (a) Raw data. (b) Raw data after applying an F-k filtering. (c) Raw data after applying a de-median filter. (d) Further processed data after applying an adaptive filter. No clipping is applied to the plotting.
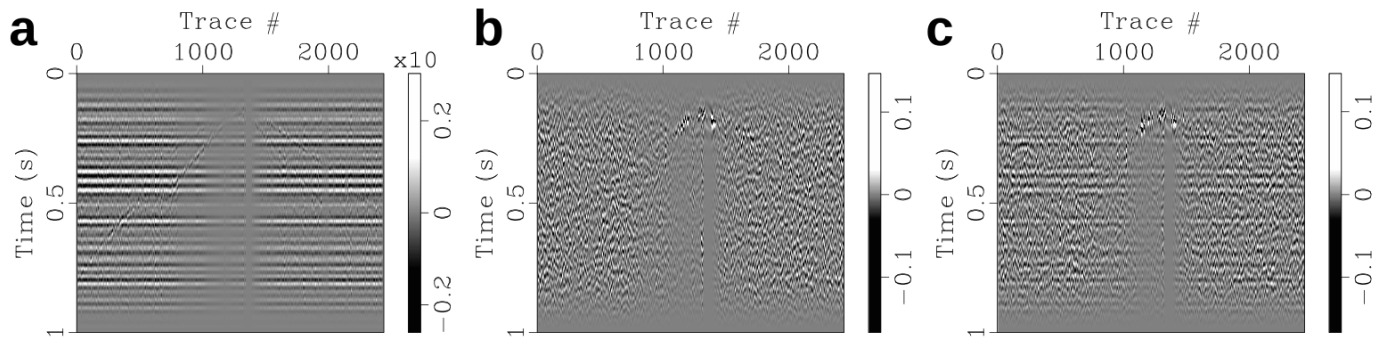


Fig. 3. Noise removed by the de-median and the adaptive subtraction filters. (a) Noise removed by the de-median filter (Figure 2a - Figure 2c). (b) Noise removed by the adaptive subtraction filter (Figure 2c -Figure 2d). (c) Noise removed by the full processing procedure (Figure 2a - Figure 2d).

where $p_i$ is the measured model parameter (Vp, Vs, and density) at depth $i$ from sonic logs, and $< p >_k$ is the parameter averaged over depths corresponding to indices between $k - h$ and $k + h$. The length of an averaging window is a fraction of the minimum dominant wavelength, which is given by $2h+1 = V_{min}/(Nf_p)$. A typical value for $N$ is 3 for practical use [52]. $f_p$ is the dominant frequency of the passing seismic waves.

Representing variables as in [54], a recipe for calculating

stiffness parameters from averaged properties of the elastic layers is given by [53]:

$$
\begin{aligned}
A &= 4\langle\tfrac{\mu(\lambda+\mu)}{\lambda+2\mu}\rangle + \langle\tfrac{1}{\lambda+2\mu}\rangle^{-1}\langle\tfrac{\lambda}{\lambda+2\mu}\rangle^2, \\
C &= \langle\tfrac{1}{\lambda+2\mu}\rangle^{-1}, \\
F &= \langle\tfrac{1}{\lambda+2\mu}\rangle^{-1}\langle\tfrac{\lambda}{\lambda+2\mu}\rangle, \\
L &= \langle\tfrac{1}{\mu}\rangle^{-1}, \\
M &= \langle\mu\rangle.
\end{aligned}
\tag{3}
$$

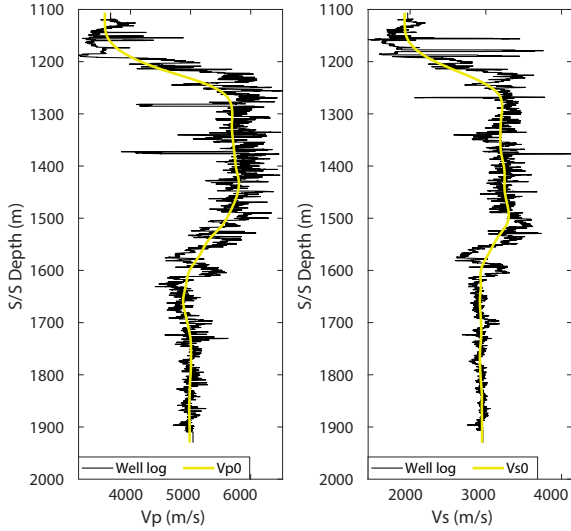Note that $\langle\cdot\rangle$ is the moving averaging mentioned in Equation

Fig. 4. Vertical P- and S-wave velocities from well-log sonic data and the Backus averaging. The depth was measured below the sea level (S/S depth). The Backus average upscale well logs to seismic wavelengths.
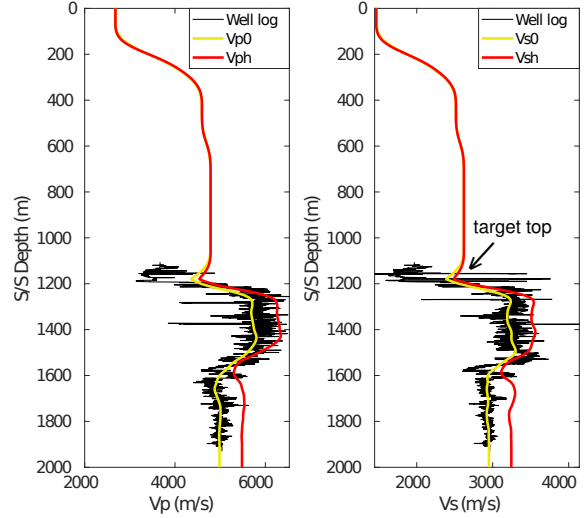


Fig. 5. Vertical and horizontal P- and S-wave velocities used for imaging. We observed strong velocity anisotropy in the target layers below 1200 m by comparing the calculated traveltime with P and S direct arrivals.

2. $\lambda$ and $\mu$ are Lamé parameters calculated from sonic logs. $A, C, F, L,$ and $M$ are notations of Love's elasticity for transversely isotropic media.

Most bulk elastic media are weakly anisotropic [55]. The Thomsen parameterization, which is a combination of two vertical wave speeds ($Vp_0$, $Vs_0$) and three dimensionless parameters ($\delta$, $\epsilon$, $\gamma$), gives an intuitive understanding of the seismic anisotropy in VTI media. It is convenient to convert the elastic stiffness parameters into Thomsen parameters:

$$
\begin{aligned}
V_{p_0} &= \sqrt{\frac{C}{\langle \rho \rangle}}, \\
V_{s_0} &= \sqrt{\frac{L}{\langle \rho \rangle}}, \\
\epsilon &= \frac{A-C}{2C}, \\
\delta &= \frac{(F+L)^2-(C-L)^2}{2C(C-L)}, \\
\gamma &= \frac{M-L}{2L}.
\end{aligned}
\tag{4}
$$

Phase velocities in weakly anisotropic media are directionally dependent (e.g., Equation 16 in [55]),

$$
\begin{aligned}
V_p(\theta) &= V_{p_0}(1 + \delta \sin^2\theta \cos^2\theta + \epsilon \sin^4\theta), \\
V_{s_v}(\theta) &= V_{s_0}\left[1 + \frac{V_{p_0}^2}{V_{s_0}^2}(\epsilon - \delta)\sin^2\theta \cos^2\theta\right], \\
V_{s_h}(\theta) &= V_{s_0}(1 + \gamma \sin^2\theta),
\end{aligned}
\tag{5}
$$

where $\theta$ is the angle between the wavefront normal and the vertical axis. $\delta$ will dominate most anisotropic effects in nearly vertical directions ($\theta \approx 0$).

Based on the depth distribution of microearthquakes and the directional preference of optical fibers, the vertical and horizontal fibers dominantly record vertically (SV waves) and horizontally (SH waves) polarized S-waves, respectively. An elliptic VTI approximation, which considers the velocity difference between horizontally and vertically propagating waves, should be able to fit the traveltime of observed P- and S-waves. To this end, we use the parameterization in terms

of $V_{p_0}$, $V_{s_0}$, $V_{p_h}$, and $V_{s_h}$ for source imaging. We calculate horizontal velocities by applying a scaling factor to the vertical ones in the target layers (Figure 5). Specifically, we divide the target reservoir into two layers and adjust the scaling factors by fitting the wavefront of direct P- and S-wave arrivals from a microearthquake (marked by the star in Figure 1b) with a well-constrained source location and relatively large magnitude. Seismic waves emitted by the perforation shots were not recorded by the fiber (they were recorded by 3C sensors), and thus, we are not able to use these data for validation. The current finding of optimal scaling factors is based on trials that aim to maximize the accumulated energy along the predicted traveltime (e.g., shown in Figure 9). The velocity of layers above the target reservoir is determined similarly. Compared with the isotropic velocity models, VTI models reduce discrepancies between predicted and observed arrival times (Figure 6) because the observed seismic waves propagate almost horizontally in the reservoir layer. The vertical S-wave velocity derived from the well log cannot accurately predict the traveltime of the SH-wave recorded by the horizontal optical fiber.

## V. ELASTIC GEOMETRIC-MEAN REVERSE TIME MIGRATION

In this paper, we use Geometric-mean Reverse Time Migration (GmRTM; [18]) with the impedance-kernel (also known as the energy-norm) imaging condition [56], [57] and a receiver grouping strategy [58], [59] for improving computational efficiency and image resolution. We use the adjoint form of the first-order elastic wave equation to extrapolate the receiver wavefield in the reverse time direction [60], [61]:

$$
\begin{pmatrix} \rho \mathbf{I}_3 & 0 \\ 0 & \mathbf{C}^{-1} \end{pmatrix} \frac{\partial \Psi}{\partial(-t)} + \begin{pmatrix} 0 & E^T \\ E & 0 \end{pmatrix} \Psi = -\mathbf{d}_k, \tag{6}
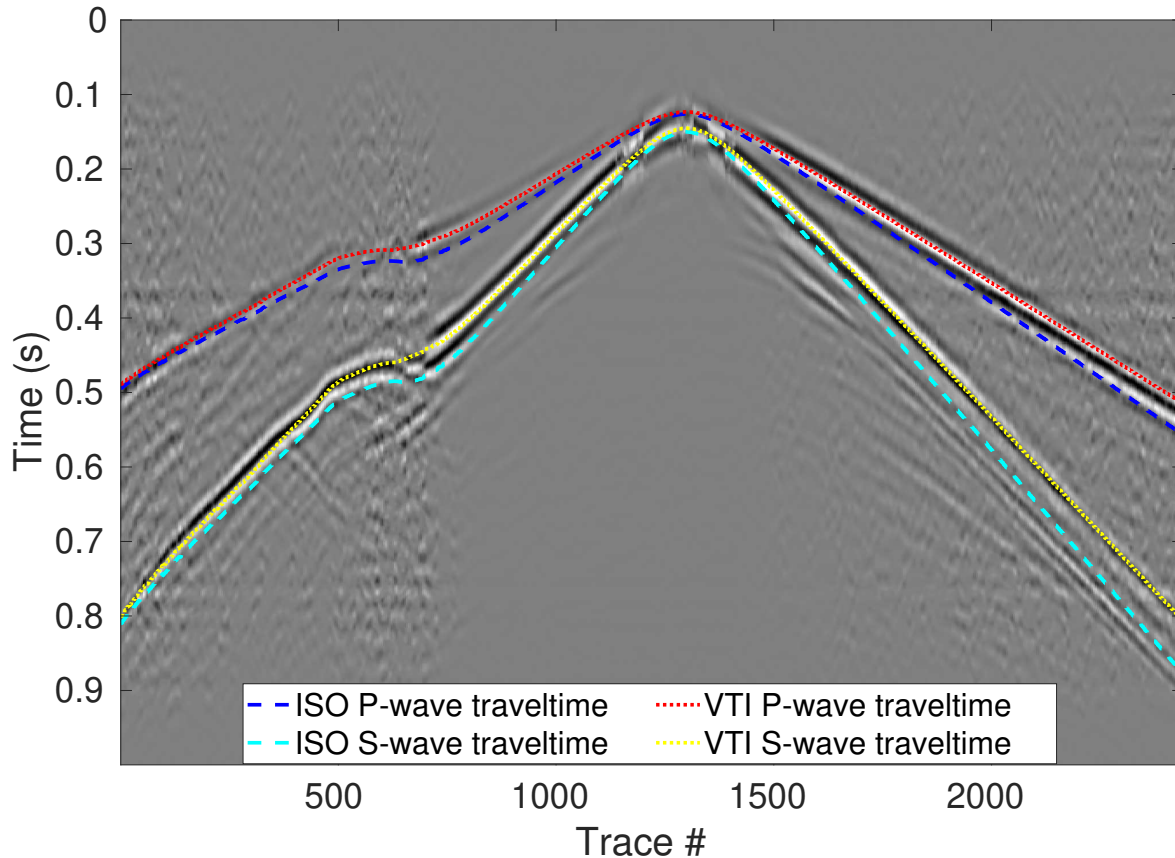$$

Fig. 6. Predicted traveltimes from isotropy and VTI models. Seismic waves propagate faster horizontally than vertically, which is usually the case due to the gravity layering of shales. The predicted traveltime by considering anisotropy matches the wavefronts of observed P and S waves well.

where $\Psi = (v_1, v_2, v_3, \sigma_1, \sigma_2, \sigma_3, \sigma_4, \sigma_5, \sigma_6)^T$ is a vector containing three particle velocities and six stress components, $E$ denotes the spatial finite-differentiation operator, $\mathbf{I}_3$ is a 3-by-3 identity matrix, $\mathbf{C}$ represents the stiffness matrix, and $\mathbf{d}_k$ denotes the $k^{\text{th}}$ group of recorded data used for reconstructing the backpropagated wavefield. There are no overlapping traces in subgroups.

We divide the DAS channels into six groups and back-propagate the recorded wavefield using a staggered-grid finite-difference solver to solve the elastic wave equation [62] with parallel computing strategies applied. The computational cost is linearly dependent on the number of subgroups and could be further reduced by using precalculated Green functions [63]. The optimal grouping strategy seeks a balance between the coherency of seismic wavefields in each subgroup and the spatial resolution of the final image [58]. Backpropagated wavefields from different receiver groups account for scatterers and constructively interfere at the location of the primary source. The image voxel with maximum amplitude after stacking is taken to be the locations of the microearthquakes.

The impedance-kernel imaging condition effectively suppresses energy from waves with large opening angles, thereby mitigating the effects of wide-angle scatterers and edge artifacts caused by the limited recording aperture, which contributes to the high-resolution images we obtain. Generally,

the impedance-kernel imaging condition is determined by weighted summation of the zero-lag cross-correlation (i.e., dot-product) of forward- and backpropagated displacement or strain fields [56], [57], [64]. For our imaging condition, we calculate the weighted summation of dot products of backpropagated displacement or strain fields (summation of Equations 14 and 15 in [64]):

$$\text{SI} = -\sum_{t=0}^{T} \{\rho(\mathbf{x}) \prod_{g=1}^{n} \mathbf{v}^g(\mathbf{x}, T-t)+ \tag{7}$$
$$C_{ij}(\mathbf{x}) \prod_{g=1}^{n} \epsilon_{ij}^g(\mathbf{x}, T-t)\},$$

in which SI denotes the source image. $\mathbf{v}^g$ is the adjoint particle velocity wavefield of the $g^{\text{th}}$ receiver group, $\epsilon_{ij}^g$ is element $ij$ of the adjoint infinitesimal strain tensor, and the Einstein summation convention over repeated indices is implied. Here we only consider the same component of the adjoint wavefield for the six receiver groups (e.g., Figure 1b) and ignore the cross components between groups.

## VI. RELOCATION RESULTS

Using 2440 DAS channels recorded with a 2.04 m receiver interval and a 7.14 m gauge length, we image 41 events with

moment magnitudes ranging from -1.4 to 0.3 (as reported by the vendor), which occurred during a 6-hour recording period. Arrivals from five of these events are still difficult to identify in the denoised DAS data; however, they are clearly visible in recordings from the geophones. To balance the spatial image resolution and computational expense, we bandpass filter the data between 15 and 38 Hz and backpropagate the wavefield in this frequency band. Aside from the huge computational cost, utilizing high-frequency data also requires a finer velocity structure model at hand to reproduce multiple scattered waves.

Assuming the microearthquakes as point sources, we stack the imaged 3D volumes along the Z, Y, and X axes to obtain X-Y, X-Z, and Y-Z transects, respectively (Figure 7). Here we show the GmRTM images calculated from original DAS data (Figure 7a), trace-normalized DAS data (Figure 7b), and 3C geophone data (Figure 7c). We observe migration imprints due to the limited migration aperture of raw DAS and geophone data, as shown in Figures 7a and 7c. Trace-wise $l_2$-norm normalization effectively enhances the far-offset signals and thus expands the migration aperture, as shown in Figure 7b. The optical fiber is oriented in the X-Z plane with mildly wiggling in the Y direction. Some mirroring artifacts in the X-Y and Y-Z transects caused by insufficient data coverage in the Y direction contaminate the images. Mirrored focal points are symmetric across the DAS line (Y=1166 m), and both yield first arrival predictions that agree well with the observations. Small deviations in the trajectory of the DAS fiber from the X-Z plane (in the Y direction) may result in minor differences in focusing amplitudes. But the amplitude difference is also vulnerable to noise and thus is unsuitable for delineating the actual source location. We use the primary particle motions derived from the 3C geophone data to eliminate the location ambiguity in the Y direction. Figures 8a and 8b are the X- and Y-component waveforms recorded by the 3C geophones deployed in the horizontal well. Along with the relatively accurate source location in X, we can estimate the incident angle of primary waves from their particle motions (Figure 8c). The linearity of the particle motion indicates that the measured waves are P-waves and the wave propagates in the same direction as the particle motions. The microearthquake examined here should be on the same side as the known source (e.g., in Figure 1a) since it locates at a larger X than the geophones. Notably, the method assumes that the first arrivals (marked by red) are direct P-waves and will fail when a different type of wave arrives earlier.

To verify the accuracy of our final locations, we project the predicted traveltimes onto the waveform for visual inspection, and we also compare them to results from cataloged locations for reference (e.g., Figure 9). Here we show three relocation examples with variable magnitudes from the catalog. Similar plots for all 41 events are also available in our shared data folder. We quantify the location accuracy using the P- to S-wave energy ratios between the relocation and catalog locations ($R = E^{GmRTM}/E^{Cat.}$). The P- or S-wave energies were calculated by integrating trace-normalized waveform envelopes along the predicted traveltimes from a VTI eikonal solver. We add trivial origin times (T0) to the predictions to account for unknown source times. The obtained ratios with
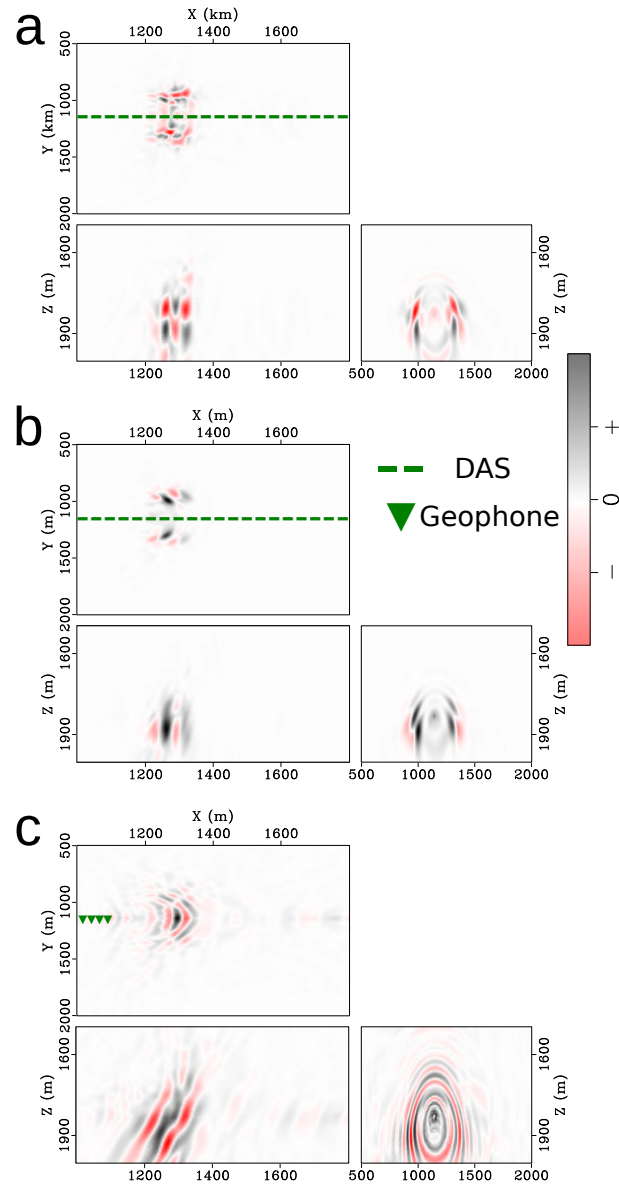


Fig. 7. X-Y, X-Z, and Y-Z panels of GmRTM images calculated from a) raw DAS data, b) Trace-normalized DAS data, and c) 3C geophone data for the back projection. We observe migration imprints from a) and c) due to the limited migration aperture. All three of these images show mirrored source images over the acquisition line.

values greater than 1 indicate the new locations, in general, yield stronger energy focusing than cataloged locations (e.g., Figures 9a and 9b). However, energy ratios smaller than 1 do not necessarily mean an inaccurate relocation result as indicated by Figure 9c, in which case the noise level is high. The signal-to-noise ratio of DAS data is also positively correlated with the variation of collected energies using different T0. We then show the crossplots of energy ratios and energy variations color-coded with magnitudes measured from geophone data (Figure 10). Most of the sampled events are within the $\pm 10\%$ range of P- or S-energy ratios, which indicates that both the relocation and cataloged events can predict the traveltime of direct P- and S-waves with similar accuracy. In addition, the tiny events of variable magnitudes, resolved from the 3C
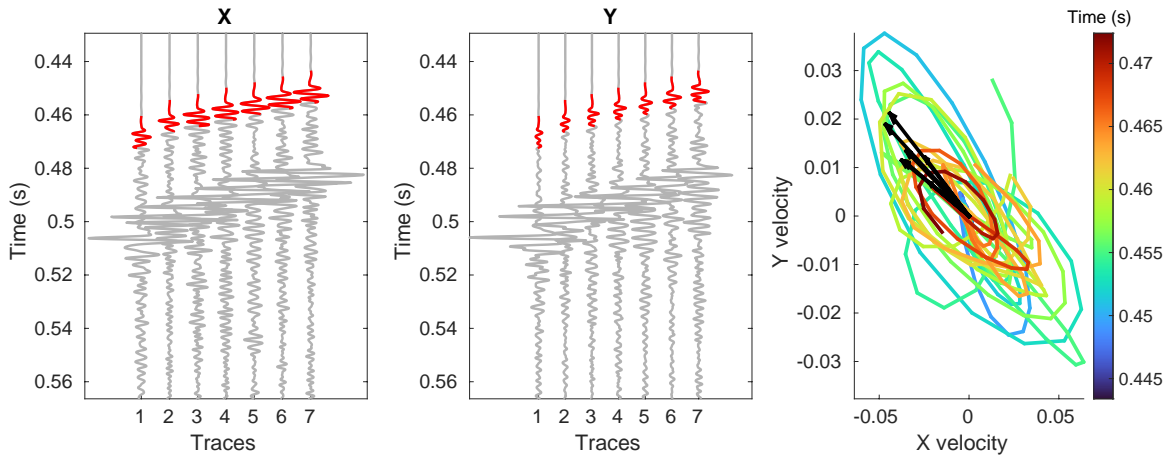
Fig. 8. Particle motions of the primary arrivals projected to the X-Y plane. The first two panels show the waveform data recorded by the 3C receivers deployed in the horizontal well. The last panel shows the calculated particle motions from the waveform segments marked red. The black arrows indicate the principal eigenvectors of different traces (scaled for visualization).

geophone data, are not separable from the calculated energy variations using DAS data, which also indicates that DAS recordings have a higher noise level than the geophone data in the same condition.

In general, our new locations cluster near the previously cataloged locations (Figure 11) and are centered near the location of perforations in the X-direction. Relocated microearthquakes diffuse vertically more than the cataloged locations, yielding greater agreement with recent laboratory observations that indicate that detectable acoustic-emission events in the Montney Formation are more diffuse than those observed in other highly brittle rocks [65]. Because previously cataloged locations were estimated using sparse borehole geophone sensors, which have limited aperture in Y and Z directions, the corresponding coordinates of these locations are relatively poorly constrained. Thanks to the vertically installed fibers, our relocated results should have a better depth accuracy than horizontal. The particle motion of P-waves derived from the 3C geophone data adds additional constraints to locations in the Y-direction. Furthermore, as shown in Figure 11d, the relocation distance generally does not strongly depend on the magnitudes, thanks to the stacking of multiple traces in the imaging process. Our new location and the cataloged location can predict the traveltime at similar accuracy as indicated by Figure 10. However, their spatial locations are significantly different. We further investigate the spatiotemporal distribution of relocated and cataloged microearthquakes in Figure 12. Our relocated earthquakes origin time and location agreed with the corresponding stage in the fracking schedule (fracking alternates between wells roughly every four hours). The earlier cluster occurs near well A, where an early stage of fracking was performed, and the latter cluster occurs near well B, where a later stage of fracking was performed (Figure 12a). Note that the identified microearthquakes shown here may occur due to earlier fracking stages (marked by void stars). The cataloged microearthquakes show similar clustering patterns in space and time. However, spatial locations for two cataloged events marked by a black oval (Figure 12b) are suspicious.

The joint DAS and geophone data relocation method, as we proposed here, should constrain the spatial location better since we use dense observations and more complete physics than conventional traveltime analysis.

## VII. SENSITIVITY OF DATA TO SOURCE LOCATIONS

Data sensitivity analysis provides insight into the uncertainty of new locations. Because energy from direct P- and S-wave arrivals dominate our GmRTM images, we can approximate Frechét derivatives of the waveform data by traveltime derivatives with respect to source location coordinates. Assuming homogeneous velocity structure, the traveltime, $T$, for an event located at $x_0$, $y_0$, $z_0$ (e.g., the star in Figure 1b) to a receiver at $x$, $y$, $z$ is given by

$$T(x,y,z) = \frac{\sqrt{(x-x_0)^2 + (y-y_0)^2 + (z-z_0)^2}}{v}, \quad (8)$$

in which $v$ is a constant velocity (set equal to 1 for simplicity). The traveltime Frechét derivatives are given by

$$\frac{\partial T}{\partial x} = \frac{x-x_0}{\sqrt{(x-x_0)^2 + (y-y_0)^2 + (z-z_0)^2}}, \quad (9)$$

$$\frac{\partial T}{\partial y} = \frac{y-y_0}{\sqrt{(x-x_0)^2 + (y-y_0)^2 + (z-z_0)^2}}, \quad (10)$$

$$\frac{\partial T}{\partial z} = \frac{z-z_0}{\sqrt{(x-x_0)^2 + (y-y_0)^2 + (z-z_0)^2}}. \quad (11)$$

As expected, all DAS channels are sensitive to the variation in the X-coordinate of the source location, and the vertical segment of the DAS fiber provides the majority of the constraint on the depth coordinate of sources (Figure 13). The Y-coordinate of source locations is predominantly sensitive to channels near the source. The depth coordinate is also sensitive to these channels, although less so, which indicates that the new locations may have trade-offs in Y and Z directions if only the near-source data are used for imaging. The summation of absolute values of Frechét derivatives also confirms that the X coordinate is the best-constrained, and the Y coordinate is the most weakly constrained. The Frechét
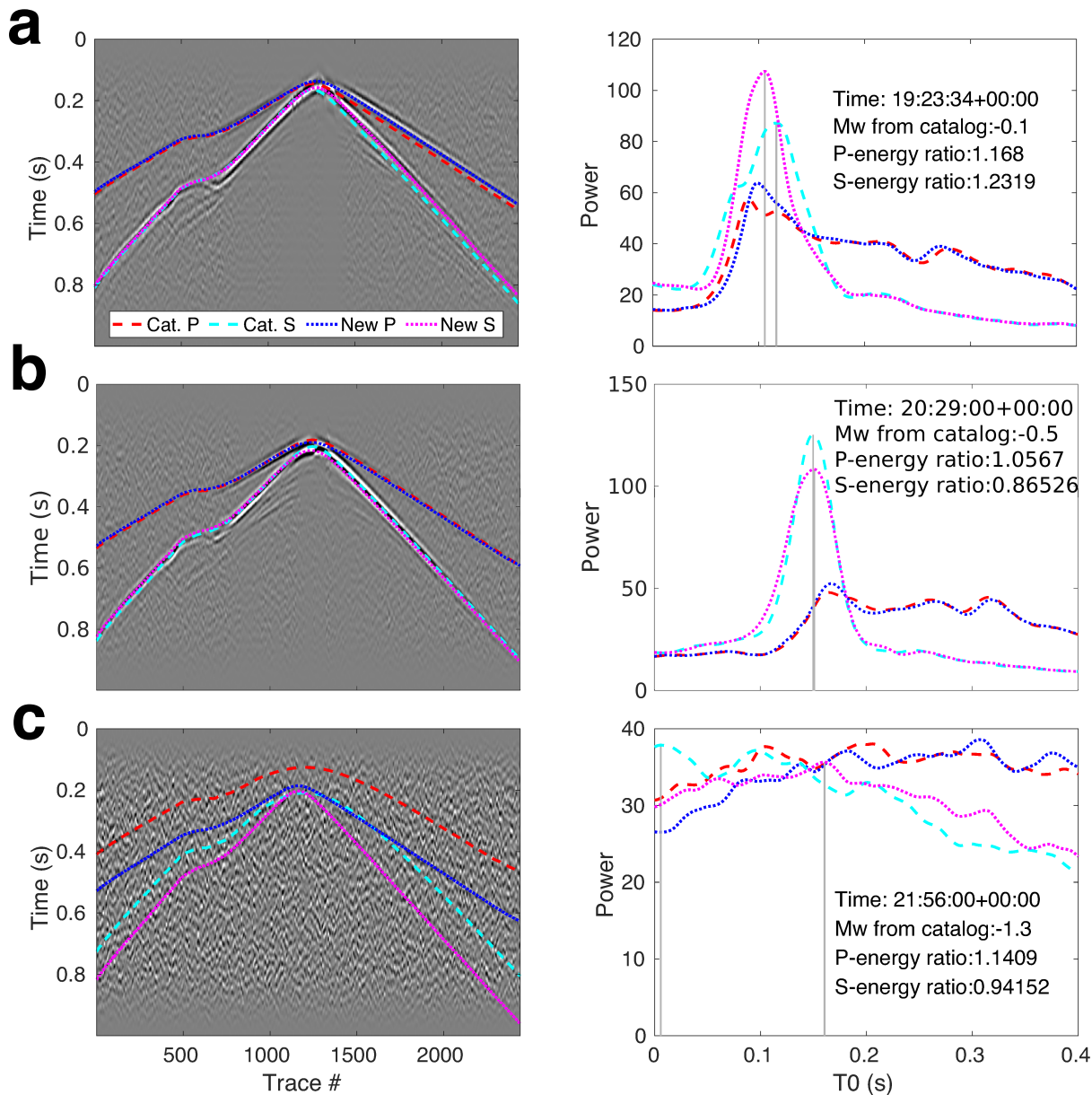
Fig. 9. Validation test for the relocation accuracy a) better, b) worse, and c) neutral. Here we show three examples in which the relocation results are a) better, b) worse, and c) neutral compared with the catalog location. The predicted traveltimes are overlaid with the DAS waveform data. Collected P- and S-wave energies along those traveltime curves (with variable origin time, T0) provide quantitative measurements of the relocation accuracy. The gray lines indicate the picked T0 for P- and S-energy ratio calculation. The variation of gather energies within T0 indicates the noise level of the data.

derivatives approximated by numerical derivatives of finite-frequency seismic waves also indicate a similar result.

## VIII. DISCUSSION: SOURCE FOCAL MECHANISM ESTIMATION

Although our relocation and the original catalog location yield similar traveltime patterns (e.g., Figures 9 and 10), their spatial locations can be very different (e.g., Figure 11). The uncertainty of the original catalog location is high due to the limited data coverage and the dense DAS acquisition is key to reducing such location ambiguity. Indeed, the combination

of geophone and DAS data can further improve the accuracy of the relocation. Geophone data are often sparse in space but record the dynamic seismic wavefield with 3C measurements and high precision. DAS data, on the other hand, have dense spatial sampling but record only strain-related signals which have an angle-dependent sensitivity to incoming waves. In short, conventional 3C sensors can record more complete dynamic information of seismic wavefield than co-located fibers. Recent research works use co-located geophones and DAS channels to calibrate the recorded strain or strain rate from a DAS line [40], [66]. Efforts were also made to use
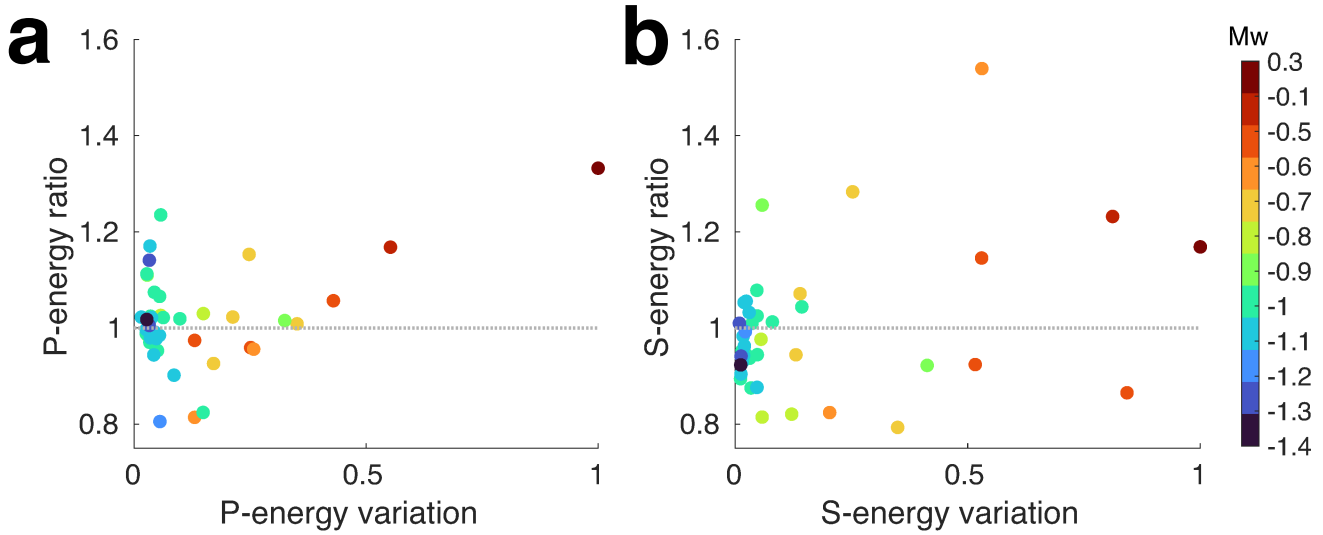
Fig. 10. Crossplots of collected energies and their variations (e.g., from Figure 9) color-coded with catalog magnitudes for a) P waves and b) S waves. Most of the events are within the $\pm 10\%$ range of energy ratios, which indicates that our relocation results have similar accuracy with the catalog in terms of matching the traveltime of direct P- and S-waves. Tiny events identified from the 3C geophone data are not separable in DAS data (energy variations are similar), which indicates that DAS recordings have a relatively larger noise level than geophone data for tiny events.
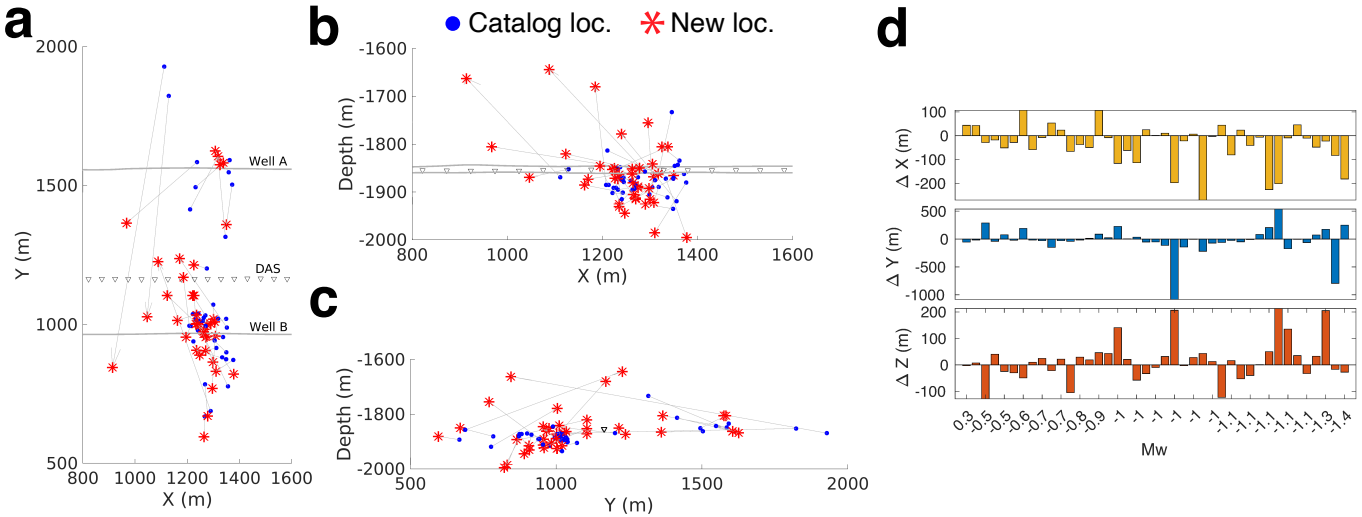


Fig. 11. GmRTM relocation migration from the catalog. They are plotted (a) in X-Y, (b) X-Z, and (c) Y-Z panels. The relocation distances for each event are shown in d). In general, the migration distance in X and Z directions are in a similar level: Both are smaller than the migration distance in Y direction (perpendicular to the 2D DAS plane).

the recorded strain for microearthquake characterization. For example, polarity flips in DAS data indicate some components of the moment tensor [32], [67]. However, practical implementations of moment tensor inversion using DAS data need to consider noise level, coupling, and gauge length on a case-by-case basis [68]. Here, we analyze the feasibility of combining geophone and DAS data for estimating the centroid-moment tensor (CMT) from the three-component (3C) geophone data.

With the best estimate of source locations, we can further estimate the source focal mechanisms using 3C geophone data. Stated most simply, given a sufficiently accurate earth model $\mathbf{m}$, seismic data $\mathbf{u}$ can be predicted by the momentum equation for an elastic continuum, which, in general, can be written as

[26]

$$\rho \ddot{\mathbf{u}} = \nabla \cdot (\mathbf{c} : \nabla \mathbf{u}) - \mathbf{M} \cdot \nabla \delta(\mathbf{x} - \mathbf{x}_s) S(t), \qquad (12)$$

in which $\mathbf{u}$ is the displacement measured at a receiver located at $\mathbf{x}_s$, $\mathbf{M}$ is the moment tensor, $S$ is termed the source time function, and $\{\mathbf{M}, \mathbf{x}_s, S\}$ is the source model used for numerical simulations.

Using the adjoint-state method, [26] derived the gradient for each component of the moment tensor $\mathbf{M}$, which is an adjoint approximation to the formal inverse problem,

$$\triangle M_{ij} = -\sum_{t=0}^{T} \epsilon_{ij}(\mathbf{x}_s, T-t) S(T - 2t_0 - t) dt, \qquad (13)$$

where $\epsilon_{ij}$ is the adjoint strain tensor recorded at the source location $\mathbf{x}_s$. The adjoint solution cannot accurately estimate
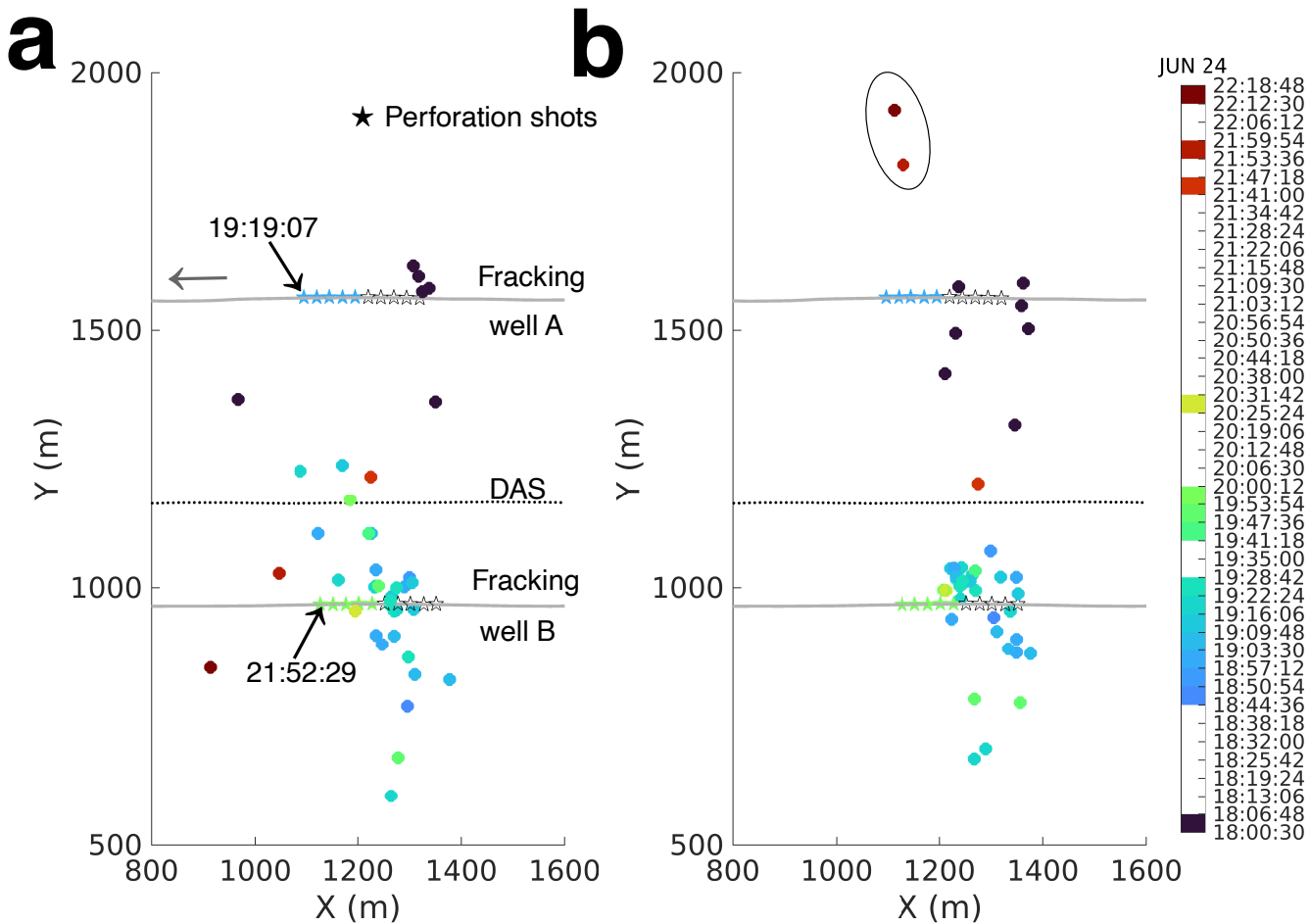
Fig. 12. Microseismic locations color-coded with observation time. a) GmRTM relocation and b) catalog location. The fracking was operated in A and B well alternatively. Arrows with time indicate the starting time of the last fracking in two stages. Void stars indicate perforation shots performed in earlier stages. The arrow along well A indicates the moving direction of perforation wells. The oval marks two suspicious catalog events in space and time.

the seismic moment $M_0$ but can provide reasonably accurate estimates for the relative values of the moment tensor.

We propose to use the estimated source location $\mathbf{x}_s$ from DAS and 3C geophone data as the first step for source mechanism estimation. Then we extract the adjoint strain (or stress) wavefield at the source location by injecting the 3C geophone data. We use a Gaussian function calculated from fitting the envelope of the adjoint strain wavefield to approximate the source time function $S$. The moment tensor can be approximated by solving Equation 13. The connection between the adjoint strain tensor and the moment tensor has also been validated through numerical examples by [69]. We use a set of synthetic tests to verify the effectiveness and accuracy of the proposed workflow. We generate the particle-velocity data using a spectral finite-element solver [70] in four scenarios: 1) A perfect geometry with the source surrounded by 26 3C receivers. 2) Same with the geometry of geophone data (Figure 1b). 3) Same with (2), but only the data component along the well tube is available. 4) Same with the geometry of DAS data. The exact locations are available in the shared data set (*/focal_mech/CMT_geometry/*). The wavefield extrapolation is based on a finite-difference scheme [62] in order to suppress the inverse crime [71]. We also assume the velocity model and source location are known in this test. Figure 14 shows

the focal mechanisms of the true and the estimated sources. The adjoint solution is reasonably close to the exact source in terms of the focal mechanism. The focal mechanism estimation seems less influenced by the azimuthal coverage of 3C sensors comparing Figures 14a and 14b. Single-component sensors, either sparsely distributed (Figure 14c) or densely distributed (i.e., DAS; Figure 14d), cannot constrain the focal mechanism inversion. The 3C geophone data is presumably more helpful for source mechanism estimation than the DAS data. A comprehensive study on the retrieval of moment tensors from borehole data was also given by [9].

The adjoint solution requires only one backpropagation of the receiver wavefield. It is the first iteration of moment tensor inversion by minimizing the waveform differences between observed and simulated seismic data, thus saving computational resources. The improvements by incorporating more iterations are limited in practice since the waveform amplitudes can be affected by many factors that are ignored in numerical simulations (as shown in [26]). There are also trade-offs between velocity and source estimation, which may degrade the source focal mechanism estimation in practice. Nevertheless, we have demonstrated sparse 3C geophone data are preferred over dense single-component DAS data for source focal mechanism estimation in an ideal case.
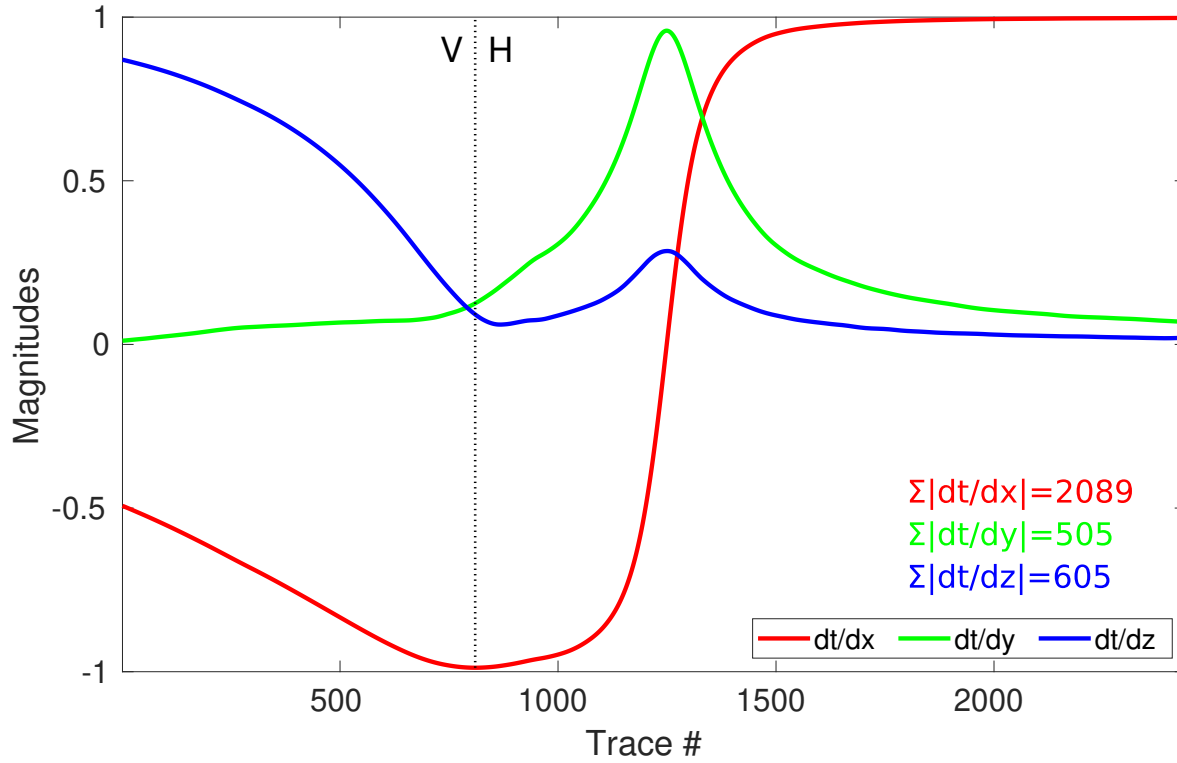
Fig. 13. Data sensitivity to source locations. The red, green, and blue lines show how the traveltime changes due to source location perturbations in X-, Y-, and Z-directions (e.g., equations 9-10). The dashed line indicates the transition between the horizontal and vertical segments of the DAS fiber. As expected, the recording data are most sensitive to X locations and least sensitive to the Y-direction. Only the near-offset data are sensitive to Y locations. However, such near-offset data have similar sensitivities to Y and Z locations, which indicates the potential trade-off between relocated Y and Z locations. The vertical section of the DAS line helps constrain the depth of relocated sources, relieving the trade-offs between Y and Z.
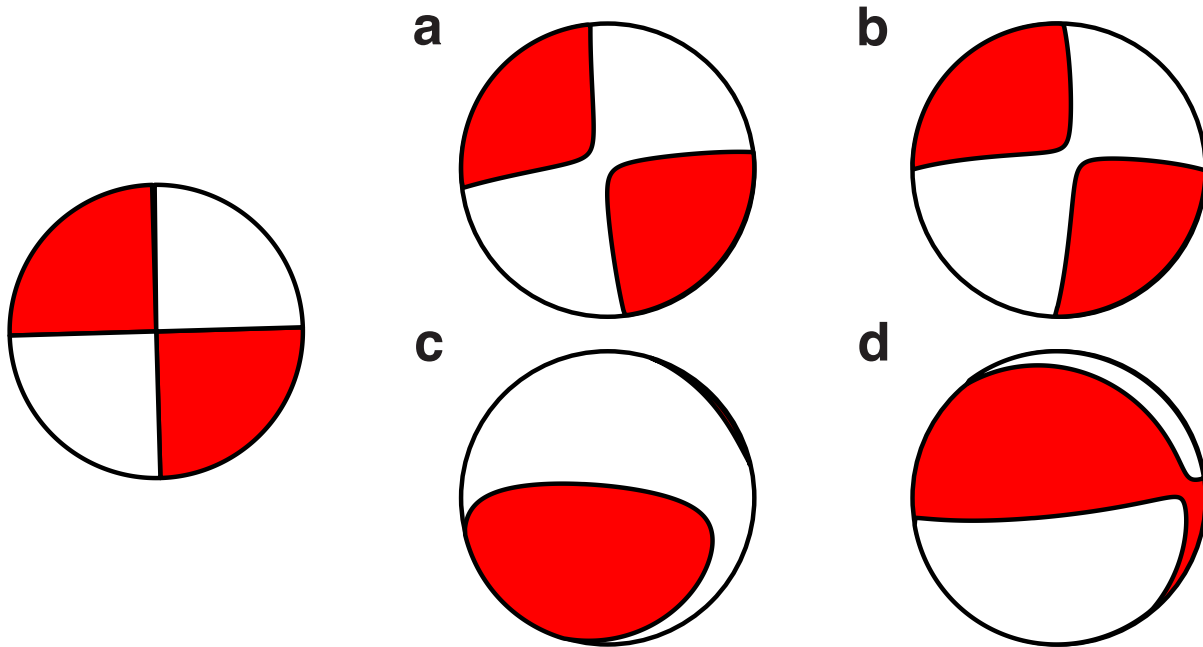


Fig. 14. True and estimated source focal mechanisms. a) Estimation from a perfect geometry. The source is surrounded by 26 3C receivers. b) Estimation from the 3C geophone data. c) Estimation from mono-component geophone data. d) Estimation from single component DAS data. We take the Z- and X-component data in the vertical and horizontal segments of the well, respectively, to mimic the DAS recording.

## IX. CONCLUSIONS

We demonstrate the feasibility of applying geometric-mean reverse-time migration to DAS data, the dense spatial sampling of which significantly benefits wavefield-based imaging. We enhance the signal-to-noise ratio of microearthquake wavefields by adaptively subtracting F-k-filtered data from the raw data, which avoids distorting the signal waveform caused by nonlinear filters. We confirm the existence of anisotropy in an unconventional shale reservoir. An elliptical VTI approximation provides sufficiently accurate kinematic information for the GmRTM imaging method used in this study. We quantify the accuracy of our new locations using the accumulated P- and S-wave energies along the predicted traveltime curves and observe that S-waves are the predominant energy source in the 41 time periods studied. Due to the limited span of optical fibers, relocated microearthquakes have significant uncertainties in directions perpendicular to the plane of fibers, where particle motions derived from 3C geophone data help remove the relocation ambiguity. We propose a two-step source inversion approach, which utilizes the dense DAS and 3C geophone data for source location estimation and the 3C geophone data for focal mechanism estimation.

## X. ACKNOWLEDGMENTS

## REFERENCES

[1] H. Clarke, L. Eisner, P. Styles, and P. Turner, "Felt seismicity associated with shale gas hydraulic fracturing: The first documented example in europe," *Geophysical Research Letters*, vol. 41, no. 23, pp. 8308–8314, 2014.

[2] F. Staněk and L. Eisner, "Seismicity induced by hydraulic fracturing in shales: A bedding plane slip model," *Journal of Geophysical Research: Solid Earth*, vol. 122, no. 10, pp. 7912–7926, 2017.

[3] T. Fischer, S. Hainzl, L. Eisner, S. A. Shapiro, and J. Le Calvez, "Microseismic signatures of hydraulic fracture growth in sediment formations: Observations and modeling," *Journal of Geophysical Research: Solid Earth*, vol. 113, no. B2, 2008.

[4] Y. Tan, J. Hu, H. Zhang, Y. Chen, J. Qian, Q. Wang, H. Zha, P. Tang, and Z. Nie, "Hydraulic fracturing induced seismicity in the southern Sichuan Basin due to fluid diffusion inferred from seismic and injection data analysis," *Geophysical Research Letters*, vol. 47, no. 4, p. e2019GL084885, 2020.

[5] H. Wang, T. Alkhalifah, U. bin Waheed, and C. Birnie, "Data-driven microseismic event localization: an application to the Oklahoma Arkoma Basin hydraulic fracturing data," *IEEE Transactions on Geoscience and Remote Sensing*, vol. early access, 2021.

[6] S. M. Mousavi, C. A. Langston, and S. P. Horton, "Automatic microseismic denoising and onset detection using the synchrosqueezed continuous wavelet transform," *Geophysics*, vol. 81, no. 4, pp. V341–V355, 2016.

[7] H. Wang and T. Alkhalifah, "Microseismic imaging using a source function independent full waveform inversion method," *Geophysical Journal International*, vol. 214, no. 1, pp. 46–57, 2018.

[8] D. Alexandrov, L. Eisner, U. b. Waheed, S. I. Kaka, and S. A. Greenhalgh, "Detection, location, and source mechanism determination with large noise variations in surface microseismic monitoring," *Geophysics*, vol. 85, no. 6, pp. KS197–KS206, 2020.

[9] V. Vavryčuk, "On the retrieval of moment tensors from borehole data," *Geophysical Prospecting*, vol. 55, no. 3, pp. 381–391, 2007.

[10] W. Menke, R. C. Holmes, and J. Xie, "On the nonuniqueness of the coupled origin time–velocity tomography problem," *Bulletin of the Seismological Society of America*, vol. 96, no. 3, pp. 1131–1139, 2006.

[11] C.-A. Murillo-Martínez and W.-M. Agudelo-Zambrano, "Sensitivity analysis of the backprojection imaging method for seismic event location," *CT&F-Ciencia, Tecnología y Futuro*, vol. 11, no. 1, pp. 21–32, 2021.

[12] R. Hull, R. Meek, H. Bello, and D. Miller, "Case history of DAS fiber-based microseismic and strain data, monitoring horizontal hydraulic stimulations using various tools to highlight physical deformation processes (Part A)," in *Unconventional Resources Technology Conference, Austin, Texas, 24-26 July 2017*. Society of Exploration Geophysicists, American Association of Petroleum, 2017, pp. 3050–3062.

[13] G. Jin and B. Roy, "Hydraulic-fracture geometry characterization using low-frequency DAS signal," *The Leading Edge*, vol. 36, no. 12, pp. 975–980, 2017.

[14] J. P. Verdon, S. A. Horne, A. Clarke, A. L. Stork, A. F. Baird, and J.-M. Kendall, "Microseismic monitoring using a fiber-optic distributed acoustic sensor array," *Geophysics*, vol. 85, no. 3, pp. KS89–KS99, 2020.

[15] G. K. Ekechukwu and J. Sharma, "Well-scale demonstration of distributed pressure sensing using fiber-optic DAS and DTS," *Scientific Reports*, vol. 11, no. 1, pp. 1–18, 2021.

[16] B. Artman, I. Podladtchikov, and B. Witten, "Source location using time-reverse imaging," *Geophysical Prospecting*, vol. 58, no. 5, pp. 861–873, 2010.

[17] M. Fink, "Time-reversal acoustics in complex environments," *Geophysics*, vol. 71, no. 4, pp. SI151–SI164, 2006.

[18] N. Nakata and G. C. Beroza, "Reverse time migration for microseismic sources using the geometric mean as an imaging condition," *Geophysics*, vol. 81, no. 2, pp. KS51–KS60, 2016.

[19] C. Song, T. Alkhalifah, and Z. Wu, "Microseismic event estimation and velocity analysis based on a source-focusing function," *Geophysics*, vol. 84, no. 3, pp. KS85–KS94, 2019.

[20] T. Zhu, J. Sun, D. Gei, J. M. Carcione, P. Cance, and C. Huang, "Hybrid multiplicative time-reversal imaging reveals the evolution of microseismic events: Theory and field-data tests," *Geophysics*, vol. 84, no. 3, pp. KS71–KS83, 2019.

[21] F. Li, T. Bai, N. Nakata, B. Lyu, and W. Song, "Efficient seismic source localization using simplified Gaussian beam time reversal imaging," *IEEE Transactions on Geoscience and Remote Sensing*, vol. 58, no. 6, pp. 4472–4478, 2020.

[22] L. Li, J. Tan, B. Schwarz, F. Staněk, N. Poiata, P. Shi, L. Diekmann, L. Eisner, and D. Gajewski, "Recent advances and challenges of waveform-based seismic location methods at multiple scales," *Reviews of Geophysics*, vol. 58, no. 1, p. e2019RG000667, 2020.

[23] Y. Chen, O. M. Saad, A. Savvaidis, Y. Chen, and S. Fomel, "3D microseismic monitoring using machine learning," *Journal of Geophysical Research: Solid Earth*, vol. 127, no. 3, p. e2021JB023842, 2022.

[24] T. Alkhalifah and Z. Wu, "Multiscattering inversion for low-model wavenumbers," *Geophysics*, vol. 81, no. 6, pp. R417–R428, 2016.

[25] Q. Liu, J. Polet, D. Komatitsch, and J. Tromp, "Spectral-element moment tensor inversions for earthquakes in southern california," *Bulletin of the Seismological Society of America*, vol. 94, no. 5, pp. 1748–1761, 2004.

[26] Y. Kim, Q. Liu, and J. Tromp, "Adjoint centroid-moment tensor inversions," *Geophysical Journal International*, vol. 186, no. 1, pp. 264–278, 2011.

[27] C. Liang, Y. Yu, Y. Yang, L. Kang, C. Yin, and F. Wu, "Joint inversion of source location and focal mechanism of microseismicity," *Geophysics*, vol. 81, no. 2, pp. KS41–KS49, 2016.

[28] R. E. Sheriff, "Factors affecting seismic amplitudes," *Geophysical prospecting*, vol. 23, no. 1, pp. 125–138, 1975.

[29] P. M. Shearer, *Introduction to seismology*. Cambridge university press, 2019.

[30] T. M. Daley, B. M. Freifeld, J. Ajo-Franklin, S. Dou, R. Pevzner, V. Shulakova, S. Kashikar, D. E. Miller, J. Goetz, J. Henninges *et al.*, "Field testing of fiber-optic distributed acoustic sensing (DAS) for subsurface seismic monitoring," *The Leading Edge*, vol. 32, no. 6, pp. 699–706, 2013.

[31] Z. Zhan, "Distributed acoustic sensing turns fiber-optic cables into sensitive seismic antennas," *Seismological Research Letters*, vol. 91, no. 1, pp. 1–15, 2020.

[32] M. Karrenbach, S. Cole, A. Ridge, K. Boone, D. Kahn, J. Rich, K. Silver, and D. Langton, "Fiber-optic distributed acoustic sensing of microseismicity, strain and temperature during hydraulic fracturing," *Geophysics*, vol. 84, no. 1, pp. D11–D23, 2019.

[33] A. Baird, A. Stork, S. Horne, G. Naldrett, J.-M. Kendall, J. Wookey, J. Verdon, and A. Clarke, "Characteristics of microseismic data recorded by distributed acoustic sensing systems in anisotropic media," *Geophysics*, vol. 85, no. 4, pp. KS139–KS147, 2020.

[34] Z.-d. Zhang, M. Alajami, and T. Alkhalifah, "Wave-equation dispersion spectrum inversion for near-surface characterization using fibre-optics acquisition," *Geophysical Journal International*, vol. 222, no. 2, pp. 907–918, 2020.

[35] T. Zhu, J. Shen, and E. R. Martin, "Sensing Earth and environment dynamics by telecommunication fiber-optic sensors: an urban experiment in Pennsylvania, USA," *Solid Earth*, vol. 12, no. 1, pp. 219–235, 2021.

[36] H. Chang and N. Nakata, "Investigation of time-lapse changes with DAS borehole data at the Brady geothermal field using deconvolution interferometry," *Remote Sensing*, vol. 14, no. 1, p. 185, 2022.

[37] S. Wu, Y. Wang, and X. Liang, "Time-delay estimation of microseismic das data using band-limited phase-only correlation," *IEEE Transactions on Geoscience and Remote Sensing*, 2022.

[38] N. J. Lindsey, H. Rademacher, and J. B. Ajo-Franklin, "On the broadband instrument response of fiber-optic DAS arrays," *Journal of Geophysical Research: Solid Earth*, vol. 125, no. 2, p. e2019JB018145, 2020.

[39] A. Fichtner, A. Bogris, T. Nikas, D. Bowden, K. Lentas, N. S. Melis, C. Simos, I. Simos, and K. Smolinski, "Theory of phase transmission fibre-optic deformation sensing," *Geophysical Journal International*, vol. 231, no. 2, pp. 1031–1039, 2022.

[40] I. Lior, A. Sladen, D. Mercerat, J.-P. Ampuero, D. Rivet, and S. Sambolian, "Strain to ground motion conversion of distributed acoustic sensing data for earthquake magnitude and stress drop determination," *Solid Earth*, vol. 12, no. 6, pp. 1421–1442, 2021.

[41] B. Olofsson and A. Martinez, "Validation of DAS data integrity against standard geophones—DAS field test at Aquistore site," *The Leading Edge*, vol. 36, no. 12, pp. 981–986, 2017.

[42] J. Atterholt, Z. Zhan, Z. Shen, and Z. Li, "A unified wavefield-partitioning approach for distributed acoustic sensing," *Geophysical Journal International*, vol. 228, no. 2, pp. 1410–1418, 2022.

[43] L. Yang, S. Fomel, S. Wang, X. Chen, W. Chen, O. M. Saad, and Y. Chen, "Denoising of distributed acoustic sensing data using supervised deep learning," *Geophysics*, vol. 88, no. 1, pp. WA91–WA104.

[44] C. J. Schenk, T. J. Mercier, M. E. Tennyson, T. M. Finn, C. A. Woodall, P. A. Le, M. E. Brownfield, K. R. Marra, and H. M. Leathers-Miller, "Assessment of continuous gas resources in the Montney and Doig Formations, Alberta Basin Province, Canada, 2018," US Geological Survey, Tech. Rep. 2018-3071, 2019.

[45] K. Sekine, C. Singh, and S. Hara, "Fracture optimization study in the Montney tight sand play," *Journal of the Japanese Association for Petroleum Technology*, vol. 81, no. 6, pp. 479–488, 2016.

[46] P. Wozniakowska and D. W. Eaton, "Machine learning-based analysis of geological susceptibility to induced seismicity in the Montney Formation, Canada," *Geophysical Research Letters*, vol. 47, no. 22, p. e2020GL089651, 2020.

[47] M. Ichikawa, S. Uchida, M. Katou, I. Kurosawa, K. Tamura, A. Kato, Y. Ito, M. de Groot, and S. Hara, "Case study of hydraulic fracture monitoring using multiwell integrated analysis based on low-frequency DAS data," *The Leading Edge*, vol. 39, no. 11, pp. 794–800, 2020.

[48] J. Ajo-Franklin, V. Rodríguez Tribaldos, A. Nayak, F. Cheng, R. Mellors, B. Chi, T. Wood, M. Robertson, C. Rotermund, E. Matzel *et al.*, "The imperial valley dark fiber project: toward seismic studies using DAS and telecom infrastructure for geothermal applications," *Seismological Society of America*, vol. 93, no. 5, pp. 2906–2919, 2022.

[49] M. P. A. van den Ende and J.-P. Ampuero, "Evaluating seismic beamforming capabilities of distributed acoustic sensing arrays," *Solid Earth*, vol. 12, no. 4, pp. 915–934, 2021. [Online]. Available: https://se.copernicus.org/articles/12/915/2021/

[50] S. Fomel, "Adaptive multiple subtraction using regularized nonstationary regression," *Geophysics*, vol. 74, no. 1, pp. V25–V33, 2009.

[51] P. Y. Cholach and D. R. Schmitt, "Intrinsic elasticity of a textured transversely isotropic muscovite aggregate: Comparisons to the seismic anisotropy of schists and shales," *Journal of Geophysical Research: Solid Earth*, vol. 111, no. B9, 2006.

[52] C. L. Liner and T. W. Fei, "Layer-induced seismic anisotropy from full-wave sonic logs: Theory, application, and validation," *Geophysics*, vol. 71, no. 6, pp. D183–D190, 2006.

[53] G. E. Backus, "Long-wave elastic anisotropy produced by horizontal layering," *Journal of Geophysical Research*, vol. 67, no. 11, pp. 4427–4440, 1962.

[54] R. Stoneley, "The seismological implications of aeolotropy in continental structure," *Geophysical Supplements to the Monthly Notices of the Royal Astronomical Society*, vol. 5, no. 8, pp. 343–353, 1949.

[55] L. Thomsen, "Weak elastic anisotropy," *Geophysics*, vol. 51, no. 10, pp. 1954–1966, 1986.

[56] H. Zhu, Y. Luo, T. Nissen-Meyer, C. Morency, and J. Tromp, "Elastic imaging and time-lapse migration based on adjoint methods," *Geophysics*, vol. 74, no. 6, pp. WCA167–WCA177, 2009.

[57] D. Rocha, P. Sava, J. Shragge, and B. Witten, "3D passive wavefield imaging using the energy norm," *Geophysics*, vol. 84, no. 2, pp. KS13–KS27, 2019.

[58] T. Bai, B. Lyu, P. Williamson, and N. Nakata, "Receiver grouping strategies for hybrid geometric-mean reverse time migration," *Geophysics*, vol. 87, no. 2, pp. KS45–KS55, 2022.

[59] T. Bai, B. Lyu, F. Li, P. Williamson, and N. Nakata, "Elastic geometric-mean reverse-time migration for source imaging," *Geophysics*, vol. 87, no. 4, pp. 1–52, 2022.

[60] D. Vigh, K. Jiao, D. Watts, and D. Sun, "Elastic full-waveform inversion application using multicomponent measurements of seismic data collection," *Geophysics*, vol. 79, no. 2, pp. R63–R77, 2014.

[61] Z.-d. Zhang, E. Saygin, L. He, and T. Alkhalifah, "Rayleigh wave dispersion spectrum inversion across scales," *Surveys in Geophysics*, vol. 42, no. 6, pp. 1281–1303, 2021.

[62] J. Virieux, "P-SV wave propagation in heterogeneous media: Velocity-stress finite-difference method," *Geophysics*, vol. 51, no. 4, pp. 889–901, 1986.

[63] L. Sawade, L. Ding, D. Peter, H. N. Gharti, Q. Liu, M. Nettles, G. Ekström, and J. Tromp, "A preliminary green function database for Global 3-D Centroid Moment Tensor inversions," Copernicus Meetings, Tech. Rep., 2023.

[64] J. Tromp, C. Tape, and Q. Liu, "Seismic tomography, adjoint methods, time reversal and banana-doughnut kernels," *Geophysical Journal International*, vol. 160, no. 1, pp. 195–216, 2005.

[65] S. Q. Jia, R. C. Wong, and D. W. Eaton, "Characterization of damage processes in Montney siltstone under triaxial compression using acoustic emission and diagnostic imaging," *Geophysical Journal International*, vol. 228, no. 3, pp. 2005–2017, 2021.

[66] J. B. Muir and Z. Zhan, "Wavefield-based evaluation of DAS instrument response and array design," *Geophysical Journal International*, vol. 229, no. 1, pp. 21–34, 2022.

[67] B. Luo, G. Jin, and F. Stanek, "Near-field strain in distributed acoustic sensing-based microseismic observation," *Geophysics*, vol. 86, no. 5, pp. P49–P60, 2021.

[68] I. Vera Rodriguez and A. Wuestefeld, "Strain microseismics: Radiation patterns, synthetics, and moment tensor resolvability with distributed acoustic sensing in isotropic media," *Geophysics*, vol. 85, no. 3, pp. KS101–KS114, 2020.

[69] C. Finger and E. H. Saenger, "Determination of the time-dependent moment tensor using time reverse imaging," *Geophysics*, vol. 86, no. 2, pp. KS63–KS77, 2021.

[70] J. Tromp, D. Komatitsch, and Q. Liu, "Spectral-element and adjoint methods in seismology," *Communications in Computational Physics*, vol. 3, no. 1, pp. 1–32, 2008.

[71] A. Wirgin, "The inverse crime," *arXiv preprint math-ph/0401050*, 2004.